chemengineering

MDPI

Article

Computational Fluid Dynamics Modeling of the Filtration of 2D Materials Using Hollow Fiber Membranes

Arash Elahi [1] and Santanu Chaudhuri [1,2,*]

[1] Department of Chemical Engineering, University of Illinois Chicago, Chicago, IL 60607, USA
[2] Department of Civil, Materials, and Environmental Engineering, University of Illinois Chicago, Chicago, IL 60607, USA
* Correspondence: santc@uic.edu

Abstract: The current study presents a computational fluid dynamics (CFDs) model designed to simulate the microfiltration of 2D materials using hollow fiber membranes from their dispersion. Microfiltration has recently been proposed as a cost-effective strategy for 2D material production, involving a dispersion containing a permeating solute (graphene), a fouling material (non-exfoliated graphite), and the solvent. The objective of the model is to investigate the effects of fouling of flat layered structure material (graphite) on the transmembrane pressure (TMP) of the system and the filtration of the permeating solute. COMSOL Multiphysics software was used to numerically solve the coupled Navier–Stokes and mass conservation equations to simulate the flow and mass transfer in the two-dimensional domain. For the TMP calculations, we used the resistance-in-series approach to link the fouling of the foulants to the TMP behavior. The foulant particles were assumed to form a polarization layer and cake on the membrane surface, leading to the increment of the TMP of the system. We also assumed the wettability of the polymeric membrane's inner wall increases upon fouling due to the flat layered structure of the foulant, which results in the reduction in the TMP. This approach accurately reproduced the experimental TMP behavior with a Mean Absolute Error (MAE) of 0.007 psi. Furthermore, the permeation of the permeating solute was computed by incorporating a fouling-dependent membrane partition coefficient for these particles. The effects of the concentration polarization and cake formation fouling stages on the membrane partition coefficient were encapsulated into our defined model parameters, denoted as α and β, respectively. This formulation of the partition coefficient yielded permeate concentration profiles, which are in excellent agreement with the experiments. For three feed concentrations of 0.05, 0.1, and 0.3 g/L, our model reproduced the experimental permeate concentration profiles with MAEs of 0.0002, 0.0003, and 0.0022 g/L, respectively. The flexibility of this model enables the users to utilize the size and concentration-dependent α and β parameters and optimize their experimental microfiltration setups effectively.

Keywords: computational fluid dynamics; hollow fiber membrane; 2D materials; membrane partition coefficient

Citation: Elahi, A.; Chaudhuri, S. Computational Fluid Dynamics Modeling of the Filtration of 2D Materials Using Hollow Fiber Membranes. *ChemEngineering* **2023**, *7*, 108. https://doi.org/10.3390/chemengineering7060108

Academic Editor: Rajinder Pal

Received: 5 September 2023
Revised: 27 October 2023
Accepted: 2 November 2023
Published: 9 November 2023

1. Introduction

Membrane technology has attained promising ubiquity throughout various research areas and industries, e.g., water treatment [1–3], gas separation [4,5], food processing [6–9], the pharmaceutical industry [10,11], etc., due to its substantial advantages over other filtration techniques. The merits of membranes over other conventional filtration technologies are, but are not limited to, cost and energy efficiency, selectivity, environmental friendliness, and so forth [3]. Despite their significant benefits over other filtration methods, the expansive utilization of membranes is limited by several obstacles. A major impediment in the efficient operation of membranes is the fouling phenomenon caused by the deposition and accumulation of particles on the membranes' inner wall [12–15]. The fouling

leads to a reduction in the permeate flux, which reduces the efficiency of the membrane performance, significantly increases the maintenance and operating costs, and shortens the membrane's lifespan.

The energy efficiency and the environmental friendliness of membrane filtration have enabled it to enter into the growing sustainable manufacturing research areas. For example, membrane technologies have been recently used for the treatment of wastewater effluent in the food industry [16]; the recovery of the bio-sourced precursor (succinic acid) of biomolecules [17]; the recovery of the lignin, which is the among the most essential bio-fuel compounds [18]; and so forth. Recently, Downing et al. [19] extended the applications of microfiltration membranes to the isolation of 2D materials (graphene) through cross-flow filtration (CFF) for the formulation of printable graphene-based inks. The filtration process yielded monodisperse graphene dispersion, which is required to formulate printable inks and led to the printing of highly conductive thin films. Their study revealed that the separation of the graphene flakes from their polydisperse solution, containing graphene flakes and incomplete exfoliated graphites, significantly improved the energy and cost-efficiency of graphene production compared with other conventional methods. Moreover, as the isolated graphene flakes were collected from the permeate stream, this CFF demonstration avoids the waste of the permeate flow, which is often discarded. Although microfiltration is a sustainable strategy for graphene production, the fouling physics during this process are yet to be investigated. Understanding the fouling physics of graphite using reliable models assists us in reducing the fouling extent and minimizing its adverse impacts on the filtration performance.

Various models have been proposed to simulate the fouling on the membrane, e.g., film theory, the shear-induced model, resistance-in-series, Derjaguin–Landau–Verwey–Overbeek (DLVO) theory, etc. [20,21]. Among these, the resistance-in-series approach has received the most notable attention due to its capacity to accommodate different fouling physics. In this formulation, the transmembrane pressure (TMP) relates to the combination of the fouling resistances through the Darcy relation. For example, the fouling resistances stemming from the concentration polarization of the foulants, gel layer formation, pore blockage, cake formation, etc. [22–26], can be combined in the resistance-in-series formulation for the computational fluid dynamics (CFDs) simulations of microfiltration systems. However, to the best of our knowledge, no CFD model attempted to simulate the fouling of flat layered structure materials such as graphite and their effect on the TMP of the system and filtration of the permeating solute.

The previously reported CFD studies of the fouling effects on the membrane operation are not suitable for studying the effects of graphite fouling on the production of 2D materials. These models produce incorrect TMP behavior resulting from the fouling of the graphite compared with the experiments and lack formulation of the fouling effects on the filtration of the permeating solute. In this study, we proposed new formulations to explain the effects of fouling of the non-exfoliated graphite on the TMP behavior and the permeation of the permeating solute. Our current attempt to model the fouling of graphite lays the initial step to understanding the fouling physics of flat layered structure materials and sets the stage for optimizing the experimental production of 2D materials using the microfiltration technique. This manuscript is structured as follows: 1—In the Methods section, we describe our assumptions and mathematical expressions. 2—The Results and Discussion section presents the reproduction of experimental results and the impact of key simulation parameters. 3—The Conclusion section outlines the fundamental findings of the paper.

2. Methods

In this study, we employed a 2-dimensional domain to model a hollow fiber membrane. The domain, which represents the membrane's lumen side, consists of four edges corresponding to the inlet, outlet, symmetric axis, and inner wall of the membrane (Figure 1). The membrane characteristics and the experimental setup parameters are obtained from

Tables S1 and S2 of Downing's report [19]. We assumed a uniform distribution of the inlet flow to each individual fiber inside the cartridge, resulting in an inlet average velocity (U_{inlet}) of 0.65 m/s, calculated using the equation $U_{inlet} = 4Q_{inlet}/(N\pi D_f)$, where Q_{inlet} is the inlet flow rate, N is the number of fibers, and D_f is the diameter of the fiber. Given the 0.65 m/s value of mean velocity, the Reynolds number yielding through the $Re = \rho U_{inlet} D_f/\mu$ relation is 192, and, accordingly, the flow is assumed laminar.

Furthermore, we assumed that each fiber contributes equally to the permeate flux, leading to a permeate velocity (U_{perm}) of 5.5×10^{-6} m/s quantified using the $Q_{perm}/(N\pi D_f L_f)$ relation, where Q_{perm} is the experimentally set permeate flow rate and L_f is the length of the fiber. The numerical simulations were performed using COMSOL Multiphysics, version 5.5, to solve the governing equations in the axis-symmetric cylindrical (r, z) coordinate system.

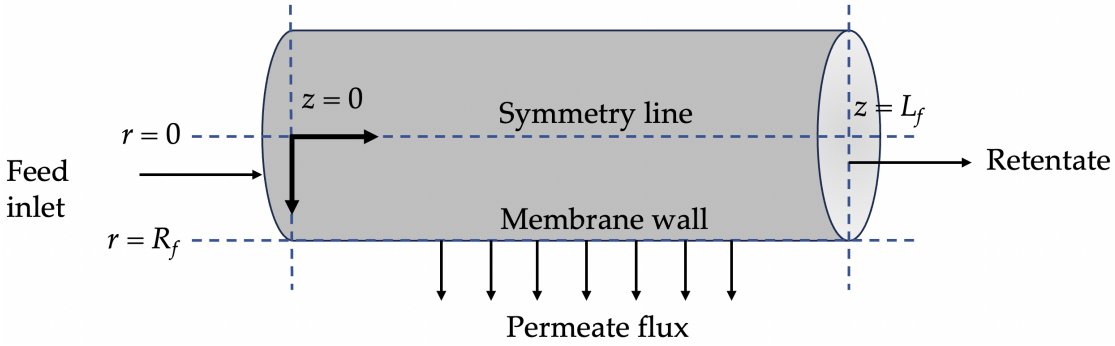

Figure 1. Schematic representation of the 2D domain for the simulation of the cylindrical hollow fiber membrane. The D_f and L_f parameters represent the radius and length of the fiber, which are 0.375 mm and 33.7 cm, respectively. For better representation, the membrane is depicted with a horizontal orientation in this figure, while in our simulation domains, the z axis aligns in the vertical direction.

2.1. Governing Equations

The velocity and pressure profiles throughout the simulation time are obtained via the numerical solving of the continuity equation (Equation (1)), Navier–Stokes in the radial direction (Equation (2)), and z-direction (Equation (3)).

$$\frac{1}{r}\frac{\partial(u_r r)}{\partial r} + \frac{\partial u_z}{\partial z} = 0 \tag{1}$$

$$\rho\left(\frac{\partial u_r}{\partial t} + u_r\frac{\partial u_r}{\partial r} + u_z\frac{\partial u_r}{\partial z}\right) = -\frac{\partial p}{\partial r} + \mu\left(\frac{1}{r}\frac{\partial}{\partial r}\left(r\frac{\partial u_r}{\partial r}\right) + \frac{\partial^2 u_r}{\partial z^2}\right) \tag{2}$$

$$\rho\left(\frac{\partial u_z}{\partial t} + u_r\frac{\partial u_z}{\partial r} + u_z\frac{\partial u_z}{\partial z}\right) = -\frac{\partial p}{\partial z} + \mu\left(\frac{1}{r}\frac{\partial}{\partial r}\left(r\frac{\partial u_z}{\partial r}\right) + \frac{\partial^2 u_z}{\partial z^2}\right) \tag{3}$$

The equations of mass conservation for the permeating (exfoliated graphene) and fouling (non-exfoliated graphite) components were coupled with the Navier–Stokes equation to determine the concentration profile of each material. The subscript i is used to denote either the permeating or fouling material.

$$\frac{\partial C_i}{\partial t} + u_r\frac{\partial C_i}{\partial r} + u_z\frac{\partial C_i}{\partial z} = D_i\left(\frac{1}{r}\frac{\partial}{\partial r}\left(r\frac{\partial C_i}{\partial r}\right) + \frac{\partial^2 C_i}{\partial z^2}\right) \tag{4}$$

The continuity and Navier–Stokes equations were subjected to the following boundary conditions. At the inlet, the flow was assumed to be fully developed.

$$\text{At } z = 0: \quad u_z = u_{z,max}\left(1 - \left(\frac{r}{R_f}\right)\right), \quad u_r = 0 \tag{5}$$

At the outlet, the atmospheric pressure assumption was applied.

$$\text{At } z = L_f: \quad P = P_{atm} \tag{6}$$

The symmetric condition was set at the centerline of the fiber.

$$\text{At } r = 0: \quad \frac{\partial u_z}{\partial r} = 0, \quad u_r = 0 \tag{7}$$

And, at the surface of the membrane, the no-slip condition was set, and the radial velocity was fixed to the permeate velocity (U_{perm})

$$\text{At } r = R_f: \quad u_z = 0, \quad u_r = U_{perm} \tag{8}$$

In addition, for both the permeating (graphene) and fouling (non-exfoliated graphite) components, the feed concentration was set to the inlet, a non-diffusive flux condition was assumed at the outlet, and the symmetric condition was applied to the centerline of the fiber.

$$\text{At } z = 0: \quad C_i = C_{i,feed} \tag{9}$$

$$\text{At } z = L_f: \quad -D_i \frac{\partial C_i}{\partial z} = -D_i \frac{\partial C_i}{\partial r} = 0 \tag{10}$$

$$\text{At } r = 0: \quad \frac{\partial C_i}{\partial r} = 0 \tag{11}$$

We assumed all the fouling particles are completely rejected at the membrane wall.

$$\text{At } r = R_f: \quad u_r C_f - D_f \frac{\partial C_f}{\partial r} = 0 \tag{12}$$

In contrast, we set the mass flux continuity boundary condition for permeating particles.

$$\text{At } r = R_f: \quad u_r C_p - D_p \frac{\partial C_p}{\partial r} = J_p \tag{13}$$

$$J_p = U_{perm} C_{p,perm} \tag{14}$$

We established a relationship between the permeating solute concentration at the permeate side ($C_{p,perm}$) and the concentration on the lumen side ($C_{p,r=R_f}$) through the definition of the membrane partition coefficient (K_{mem}) for the permeating material.

$$K_{mem} = \frac{C_{p,perm}}{C_{p,r=R_f}} \tag{15}$$

However, we postulated that the selective partitioning of permeating particles across the membrane vary in the presence of fouling. To account for this, we developed an equation for the membrane partition coefficient (K_{mem}) that takes into consideration the fouling effects. The details of this fouling-dependent equation will be elaborated in the subsequent sections.

2.2. Resistance Parameters

In the constant permeate flux setup of cross-flow filtrations of macromolecules, fouling often results in an increase in transmembrane pressure (TMP). This increment of TMP is necessary to overcome the growing resistances caused by fouling. However, the fouling of graphite led to a different TMP behavior. Through a visual inspection of the TMP profile over time for the filtration of graphene from the non-exfoliated graphite (Figure S2d of reference [19]), we detected three distinct regimes: an initial rise in TMP, a slight decline in TMP, and a stabilization in TMP. We hypothesize the initial abrupt increment in the TMP

corresponds to the formation of the polarization layer, and the final stage corresponds to pore blockage and cake formation, which are related to the TMP through Darcy relation (Equation (16)) in our formulation.

$$U_{perm} = \frac{\text{TMP}}{\mu R_{total}} \tag{16}$$

To characterize these two regimes, we adopted the formulations developed by Marcos et al. [23] to represent the resistances associated with polarization (R_{pol}) and cake formation (R_{cake}).

$$\tau_{pol} \frac{dR_{pol}}{dt} = (R_{pol,ss} - R_{pol}) \tag{17}$$

$$R_{pol}(t = 0) = 0 \tag{18}$$

The parameter $R_{pol,ss}$ corresponds to the steady-state value of polarization resistance, indicating the onset of the pore blockage and cake formation regime. The τ_{pol} is the polarization time constant and relates to the concentration of the foulants on the inner wall of the membrane through the following equation.

$$\tau_{pol} = \frac{k_{pol}}{C_{f,r=R_f}} \tag{19}$$

For the sake of more clarity, the R^*_{block} term in the Marcos et al. [23] report, which is the combined effects of pore blockage and cake formation resistances, is denoted as R_{cake} in this work. The R_{shear} accounts for shear stress in the flow, which helps wash away foulants and decrease the fouling resistance, and R_{ads} corresponds to the initial adsorption of the foulants to the inner wall membrane and blockage of the pores.

$$\tau_{cake} \frac{dR_{cake}}{dt} = (R_{cake} - R_{shear}) \tag{20}$$

$$R_{cake}(t = 0) = R_{ads} \tag{21}$$

However, the observed slight reduction in TMP during the filtration of 2D graphenes from the ethanol dispersion [19] is unique to the fouling of graphitic layered structures and has not been extensively studied before. To gain insights into this behavior, we turned to studies on graphene-coated membranes [27–34], which have yielded enhanced filtraton performance. For example, the coating of polyamide [31] and polysulfone [32] membranes with graphene oxide (GO) and the modification of the polyvinylidene fluoride membrane [33] with sulfonated graphene oxide (SGO) have been reported to reduce the surface roughness of the membrane and increase the flux rate of the permeating water. The higher flux rate of water for the coated membrane cases has been attributed to the greater hydrophilicity of GO and SGO compared with polymeric surfaces, which leads to better spreading of the water droplets on the membrane surface, and, accordingly, higher permeation rate of water molecules through the membrane pores. Moreover, it has also been reported that ethanol-containing droplets spread on the surface of pristine graphene flakes [35], and the wettability of the surface increases (contact angle decreases) with higher ethanol content [36]. Therefore, we speculate that when the graphite compounds, which are a stack of many graphene layers, foul on the inner wall of the membrane, smoother and more wettable surfaces are provided for the ethanol flow. This leads to a decrease in the contact angle between the ethanol droplets and the membrane surface, and they spread on the surface, promoting the rate of permeation of ethanol molecules through the pores. Therefore, to maintain the desired permeate flux in the constant permeate flux setup, the driving force (TMP) decreases slightly until the cake formation regime becomes dominant, at which point the TMP levels off. Thereby, to capture the effects of increased wettability of

the membrane surface upon fouling on the TMP behavior, we defined another resistance term, as below:

$$\tau_{wet}\frac{dR'_{wet}}{dt} = (R'_{wet,ss} - R'_{wet}) \tag{22}$$

Unlike the R_{pol} and R_{cake} parameters, which indicate increased membrane resistances to permeate flow, the R'_{wet} parameter reflects enhanced permeate flow through the membrane pores due to improved wettability resulting from fouling by flat layered structure graphite. We used the prime symbol (′) to differentiate it from the other resistance terms, as R'_{wet} opposes the effects of R_{pol} and R_{cake}, and it represents the reduction in the TMP. The $R'_{wet,ss}$ is the limit of fouling effect on the enhanced wettability before the cake formation regime takes over the control of the TMP behavior. Also, as the wettability resistance term depends on the concentration of the foulents on the membrane, we used a foulant's concentration-dependent formulation for the time constant of the wettability effects.

$$\tau_{wet} = \frac{k_{wet}}{C_{f,r=R_f}} \tag{23}$$

The total resistances used in the Darcy relation (16) to calculate the TMP are expressed in Equation (24). The R_m term represents the clean membrane resistance, which is intrinsic to the membrane's characteristics. Since the R'_{wet} term reduces the magnitude of the resistances in our formulations, it is associated with a negative sign in Equation (24).

$$R_{total} = R_m + R_{pol} + R_{block} - R'_{wet} \tag{24}$$

This equation represents the local resistance of the membrane along the z-direction, which gives rise to local TMP values according to Equation (16). However, the experimentally obtained TMP values are determined with the following equation.

$$\text{TMP} = \frac{P_{in} + P_{ret}}{2} - P_{perm} \tag{25}$$

Thus, we averaged the TMP values calculated using Equations (16)–(24) along the z-direction to compare them with the experimental data.

2.3. Permeate Flux Concentration

To determine the permeate concentration of the permeating solute (exfoliated graphene), we utilized a partition coefficient (Equation (15)). This coefficient depends on various factors, including membrane properties, solute characteristics, and thermodynamic conditions. However, in our case, the inner surface of the membrane undergoes changes during operation and fouling. As a result, we developed a fouling-dependent expression for the partition coefficient (Equation (26)), which satisfies three conditions:

(a) Accounts for the size of the permeating particles. (b) Maintains a constant partition coefficient for very small solute particles molecules, such as ions. (c) Reflects a significant decline in the partition coefficient for large particles that are completely rejected with partial pore blockage.

$$K_{mem}(t) = \frac{R^0_{pol} + R^0_{cake}}{R^0_{pol} + \alpha\left(R_{pol} - R^0_{pol}\right) + R^0_{cake} + \beta\left(R_{cake} - R^0_{cake}\right)} \tag{26}$$

The formulation introduces two parameters, α and β, which represent the ratios of rejected permeating particles to rejected ethanol molecules in the polarization and cake formation stages, respectively. When dealing with small particles like ions where $\alpha = \beta = 0$ (Figure 2a), the partition coefficient remains uniform, resembling the bulk concentration. Conversely, for larger molecules with $\alpha, \beta >> 0$ (Figure 2b), as the solvent flows towards the membrane, the particles may be rejected by the foulants during the concentration polarization or cake formation regimes, leading to a decrease in the partition coefficient.

Therefore, the fouling-dependent partition coefficient formulation (Equation (26)) accounts for changes in the membrane's inner surface, differentiates between solute sizes, and ensures the accurate calculation of the permeate concentration.

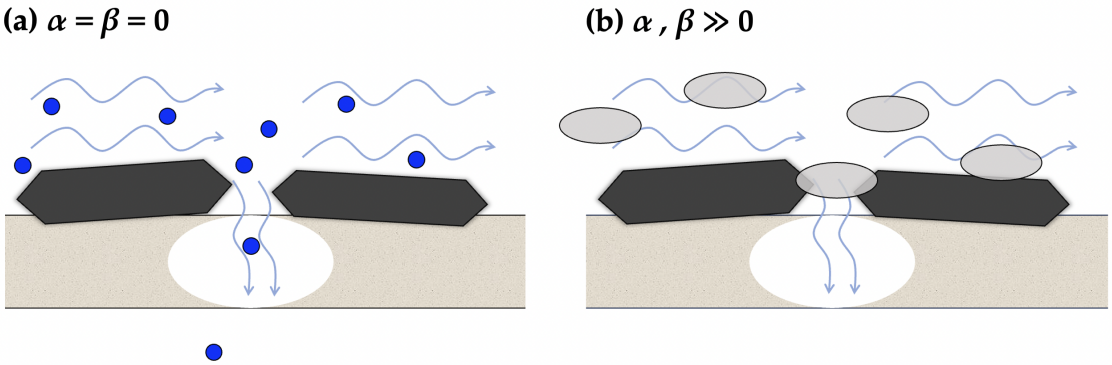

Figure 2. Effect of fouling on the permeate behavior of permeating particles. (**a**) Small particles ($\alpha = \beta = 0$) permeate through the pores with the solvent flow. (**b**) Large particles (α, $\beta >> 0$) are rejected by the reduced pore size due to the fouling, justifying the varying membrane partition coefficient for these particles. The foulant particles are colored black to represent graphite, while the colors of the permeating solutes are assigned arbitrarily.

2.4. Numerical Solution

The 2-dimensional transient formulations of Navier–Stokes and mass conservation equations were implemented using COMSOL Multiphysics (version 5.5). The weak formulations of the resistance dynamics differential equations (Equations (17), (20) and (22)) were applied on the permeate boundary ($r = R_f$). The domain was gridded using Mapped meshes (rectangular meshes). We employed mesh growth rate of 10 in the r direction to create finer meshes near the inner wall of the membrane ($r \simeq R_f$). The higher resolution was necessary for accurate numerical solving of multiple differential equations on this boundary. Our grid sensitivity test determined that the optimal mesh distribution in the 2D domain consisted of 9000 elements, with 30 and 300 elements in r ($N_{grid,r}$) and z ($N_{grid,z}$) directions, respectively (Figure 3). To match the experimental data we used for fitting the model parameters, the simulation time was fixed to 7500 s. The time step was set to 0.5 s and the convergence of the method was determined using a relative tolerance of 1×10^{-6}. The numerical simulations were carried out on a computer with an Intel Xeon processor (2.4 GHz, 6 cores), 16 GB of RAM, and a 64-bit Linux 20.04 operating system. The average CPU time for each simulation was approximately 11 min.

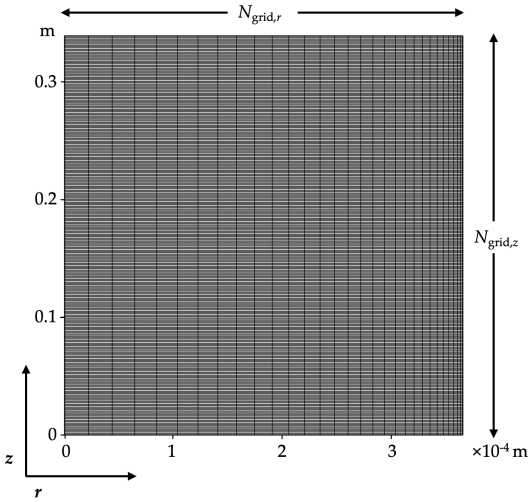

Figure 3. Optimum meshed geometry for the numerical simulations.

3. Results

The constant permeate flux setup of the membrane operation leads to the formation of flow streamlines directed almost perpendicularly to the membrane surface (Figure 4). The orientation of flow streamlines toward the membrane surface leads to the build-up of fouling components (Figure 5) near the membrane surface ($\frac{r}{R_f} \simeq 1$), which affects the driving force required (TMP) to fuel the preset permeate flow rate (U_{perm} of 5.5×10^{-6} m/s). The effects of fouling on the TMP behavior and the permeation of the permeating solute (represented by the permeate concentration profile) are coupled to the resistance dynamics equations and membrane partition coefficient, respectively. The determination of resistance and membrane partition coefficient (α and β) parameters via fitting against the experimental results is elaborated in the following sections. The experimental permeate concentration and TMP values were inherited from Figure S2c,d of reference [19].

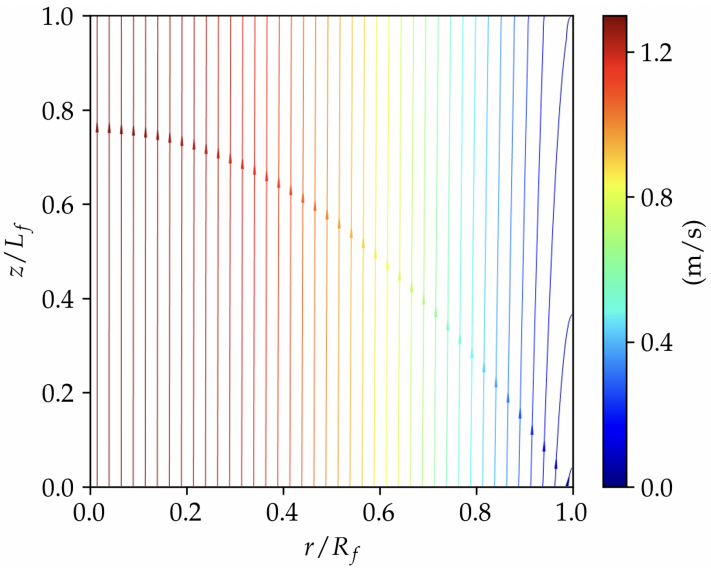

Figure 4. Streamline of fluid flow inside the hollow fiber 2D domain. The result corresponds to the final time step of the simulation using the fitted resistance parameters.

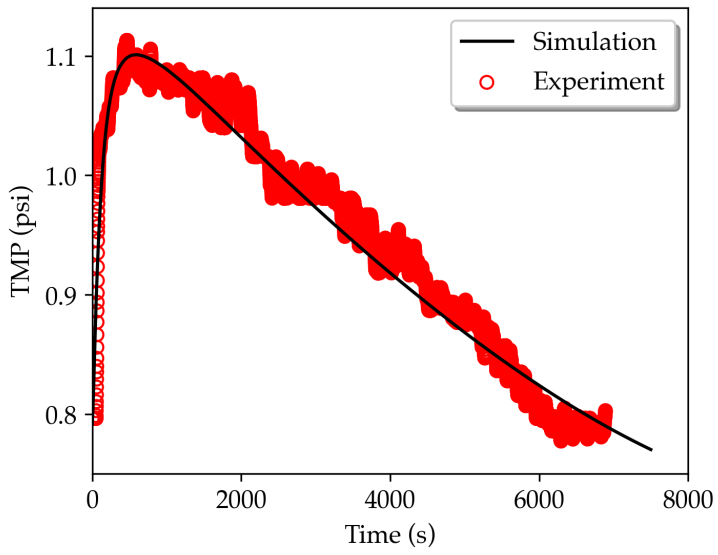

Figure 5. Concentration gradient of the fouling particle near inner the wall of membrane. The result corresponds to the final time step of the simulation using the fitted resistance parameters.

3.1. TMP Dynamics

Table 1 summarizes the resistance parameters used to reproduce experimental TMP data. The R_m value was estimated based on the previously measured hydraulic resistances for the microfiltration hollow fiber membranes (with pore sizes greater than 0.1 µm) [37–39]. These hydraulic resistance values consistently fall around the scale of 10^{11} $\frac{1}{\mathrm{m}}$. The R^0_{cake} value was deduced from the TMP value measured at the initial time step. Furthermore, we assigned a value of 2 $\times$ 10^{-3} Pa·s to the viscosity of the feed, which is the dispersion of the solid solutes in ethanol. This value was chosen to be between the viscosity of pure ethanol (1.1 $\times$ 10^{-3} Pa·s) [40] and the measured viscosity of the thickened permeate stream (approximately 2.5 $\times$ 10^{-3} Pa·s) [19]. To ensure the consistency of the experimental and simulation data, we excluded the initial 3 min of the experiment and set t = 3 min as the initial time step. By optimizing the remaining resistance parameters, we successfully captured the three stages of fouling. The optimized parameters yielded a TMP profile that closely matched the experimental results (Figure 6), with a Mean Absolute Error (MAE) of 0.007 psi (Figure 6).

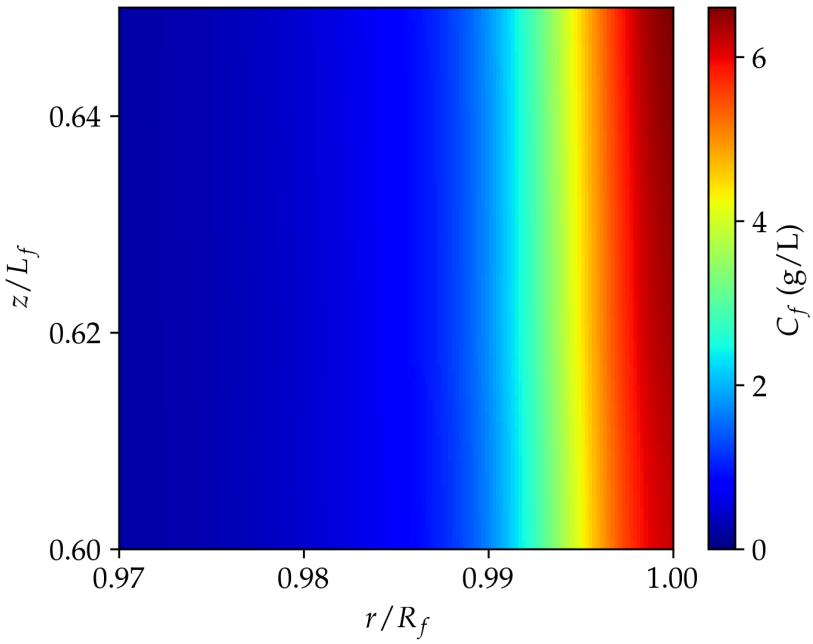

Figure 6. Variation in TMP over time obtained from experiments and simulations using optimized parameters. The experimental data are obtained from reference [19].

Table 1. Model parameters.

	System Parameters	**Value**
Membrane properties	D_f (mm)	0.75
	L_f (cm)	33.7
	N_f	20
Operating conditions	Q_{inlet} (mL/min)	343
	Q_{perm} (mL/min)	5
	U_{inlet} (m/s)	0.65
	U_{perm} (m/s)	5.5 $\times$ 10^{-6}
Solute and solvent properties	C_{feed} (g/L)	0.3
	μ (Pa·s)	2 $\times$ 10^{-3}
	ρ (kg/m^3)	789

Table 1. *Cont.*

	System Parameters	Value
Resistance parameters	R_m $(\frac{1}{\mathrm{m}})$	1×10^{11}
	k_{pol} (s g/L)	1000
	$R_{pol,ss}$ $(\frac{1}{\mathrm{m}})$	2.5×10^{11}
	k_{wet} (s g/L)	1.4×10^{5}
	$R'_{wet,ss}$ $(\frac{1}{\mathrm{m}})$	9×10^{11}
	τ_{block} (s)	2825
	R_{ads} $(\frac{1}{\mathrm{m}})$	4.20×10^{11}
	R_{shear} $(\frac{1}{\mathrm{m}})$	4.18×10^{11}

3.2. Permeating Particle Dynamics

The higher concentration of foulants in the proximity of the inner wall (Figure 5) indicates the reduction of the permeating area for the permeating particles (exfolaited graphene flakes) and, thereby, reduced membrane partition coefficient for them. Analyzing Figure 6 reveals an initial abrupt increment of the TMP value until it reaches its maximum at t = 500 s, indicating the concentration polarization regime. Subsequently, the fouling particles reduce the pore size and form a cake layer, which begins to dominate the TMP behavior at the end of the membrane operation (t > 6000 s). The effects of the polarization stage on the rejection of the permeating solute are encapsulated in the α parameter, while the β parameter represents the influence of the cake layer growth on the disruption of the solute isolation. To investigate our model's capability to capture the effects of α and β parameters on the behavior of the permeating solute at the end of the polarization regime, we examined the concentration gradient in the neighborhood of the inner wall of the membrane, i.e., $\frac{r}{R_f} \simeq 1$ (Figure 7), at t = 500 s. As Figure 7a displays, for the very small solute particles ($\alpha = \beta = 0$), the uniformity of the inlet concentration (0.075 g/L) is preserved across the domain. For the particles with larger α and β values, i.e., α = 10 and β = 10 (Figure 7b), partial rejection of the particles by the foulant compounds occurs, leading to the build-up of the permeating solute particles and elevation in the average concentration value to 0.21 g/L on the membrane wall. Further increment of the α value (α = 100, β = 10) leads to a broader concentration gradient and promotes the average concentration on the wall to 0.32 g/L (Figure 7c). However, we detected minimal impact by increasing the β value, i.e., α = 10, β = 100, (comparing Figure 7b,d) on the behavior of permeating solute rejection. Hence, during the concentration polarization stage, solute filtration is primarily controlled by the α parameter, with negligible influence from β values.

The effects of variation in the α and β parameters on the rejection behavior of permeating solute after more than 2 h, i.e., t = 7500 s, where the cake formation contribution dominates, are displayed in Figure 8. For the small particles ($\alpha = \beta = 0$), the solute distribution remains uniform until the end of the simulation (Figure 8a). With α = 10 and β = 10, there is an insignificant increment of the wall concentration of permeating solute from 0.21 g/L at t = 500 s (Figure 7a) to 0.23 g/L at t = 7500 s (Figure 8b). Increasing the α value to 100 yields an identical concentration gradient profile of permeating solute near the wall at both t = 500 s (Figure 7c) and t = 7500 s (Figure 8c). The slow dynamics of the permeating solute behavior near the wall can be attributed to the fact that for the large α values, the membrane partition coefficient converges to its lowest values at the end of the concentration polarization regime, maximizing the solute rejection. Therefore, a stable concentration boundary layer of the permeating solute is formed after the initial stage. Finally, in contrast to the minimal effects of β values on the average value of permeating solute concentration on the membrane wall at t = 500 s (comparing Figure 7b,d), raising the β value to 100 promoted the wall concentration of the permeating solute to 0.27 g/L (Figure 8d) compared with the 0.21 g/L obtained for the β = 10 case at the end of the simulation (Figure 8b). Therefore, our results suggest that the α parameter determines the

level of permeating solute rejection during the concentration polarization regime, while the β values control the rejection during the cake formation stage.

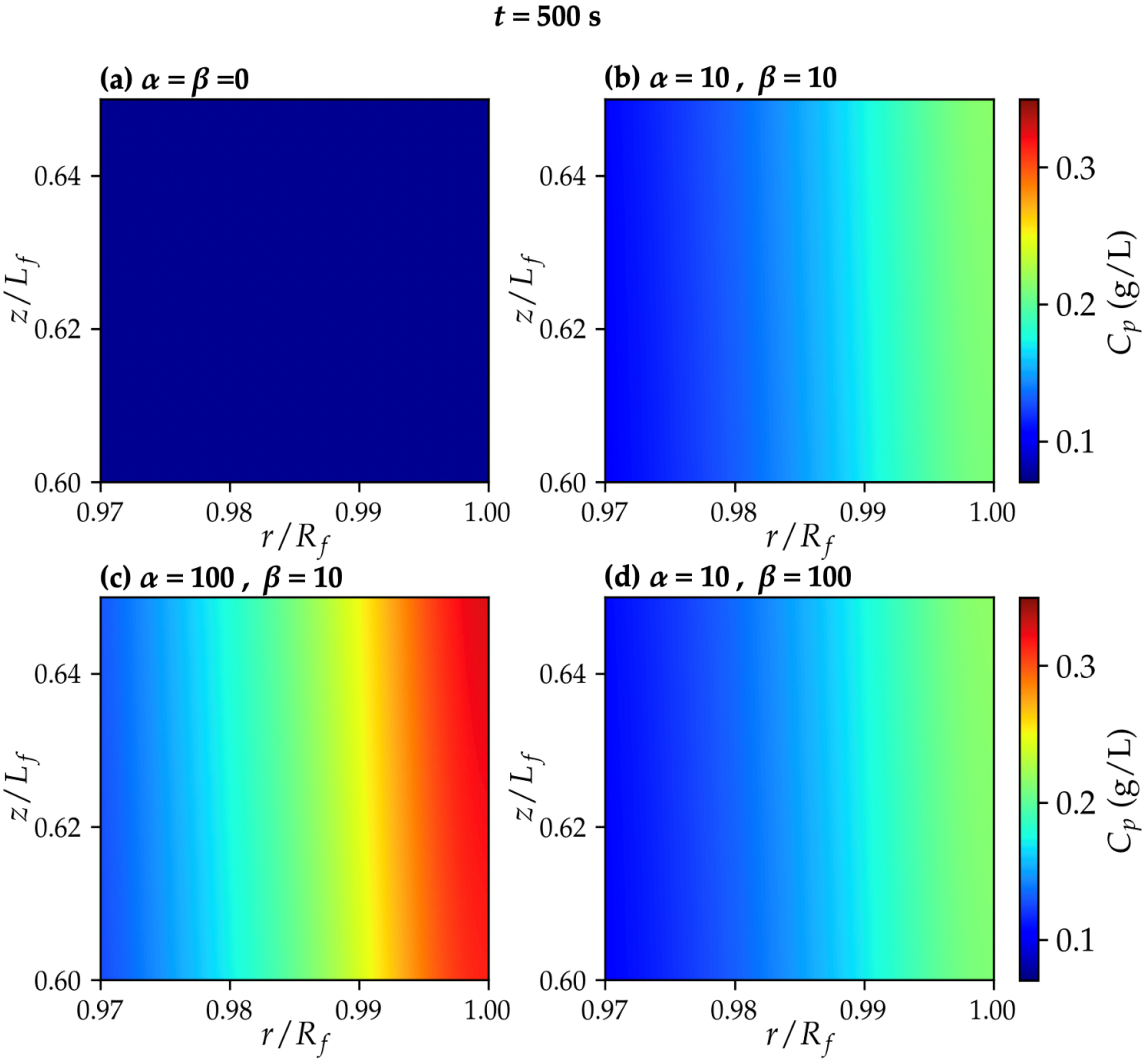

Figure 7. Concentration gradient of permeating solute at t = 500 s for (**a**) $\alpha = \beta = 0$, (**b**) α = 10 and β = 10, (**c**) α = 100 and β = 10, (**d**) and α = 10 and β = 100.

To further understand the effects of the α and β parameters on membrane characteristics, we examined the variation in the relative membrane partition coefficient ($\frac{K_{perm}}{K^0_{perm}}$) over time (Figure 9a), where K^0_{perm} is the initial partition coefficient. As mentioned earlier, the particles with $\alpha = \beta = 0$ impose no impacts on the membrane characteristics, resulting in a constant partition coefficient (red plot). For the case with the highest α value (α = 100), the non-dimensional partition coefficient mitigates to 0.024 after 500 s and remains nearly constant (green plot). The two simulations for the α = 10 case initially exhibited identical partition coefficient behaviors (until t = 500 s), but diverged over time, with a slight decline in the case with β = 10 (blue plot) and a steeper descent in the case with β = 100 (purple plot).

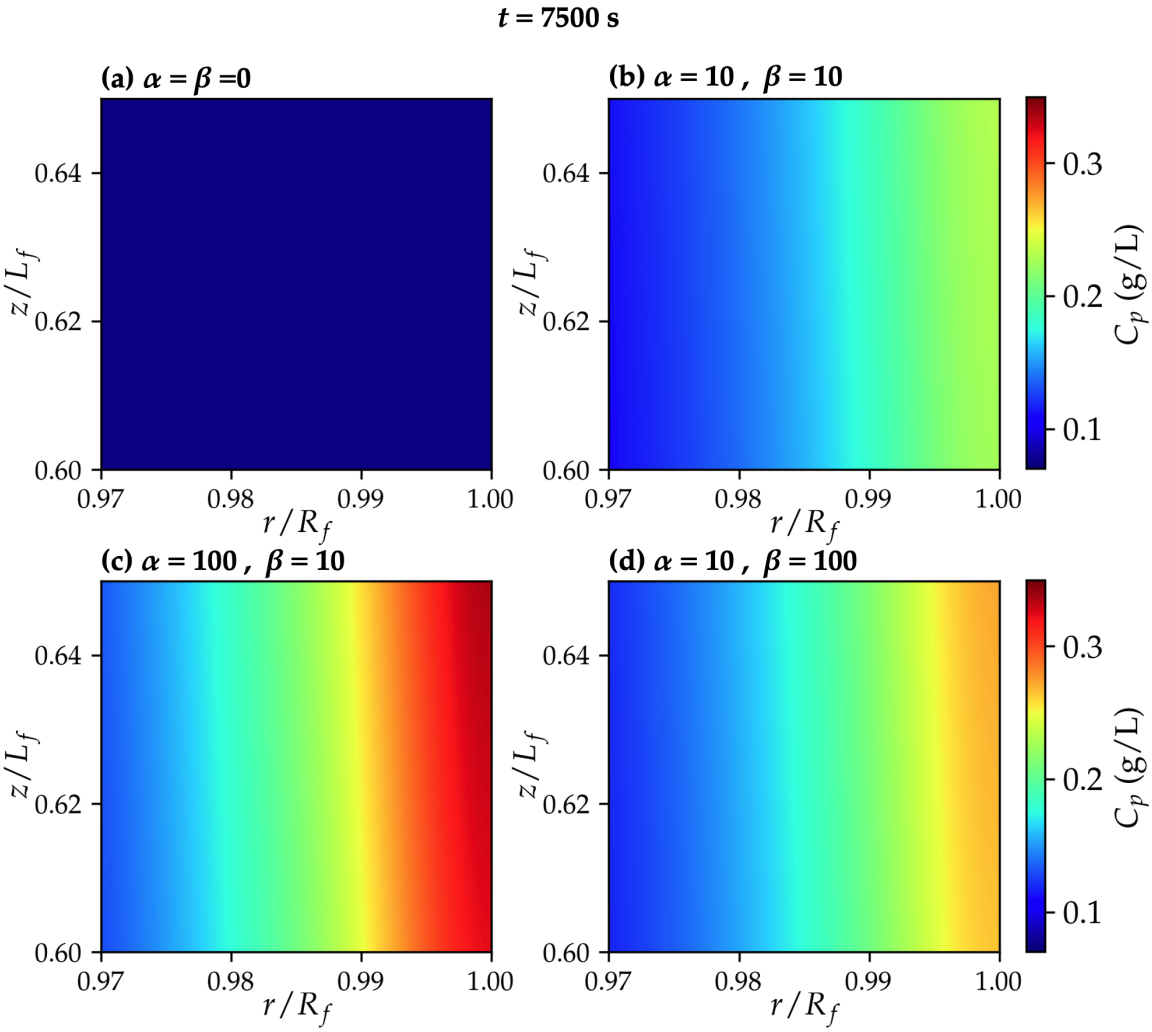

Figure 8. Concentration gradient of permeating solute at t = 7500 s for (**a**) $\alpha = \beta = 0$, (**b**) $\alpha = 10$ and $\beta = 10$, (**c**) $\alpha = 100$ and $\beta = 10$, (**d**) and $\alpha = 10$ and $\beta = 100$.

The permeating solute concentration profile at the permeate stream is driven from the membrane partition coefficient and the wall concentration of the permeating solute (on the lumen side) using Equation (15). Figure 9b demonstrates that the non-dimensional permeate concentration ($\frac{C_{p,perm}}{C^0_{p,perm}}$) profile follows a similar pattern to the membrane partition coefficient. However, except for the $\alpha = \beta = 0$ case, where the non-dimensional permeate concentration remains unified throughout the operation time, the permeate concentration is shifted upward compared with the membrane partition coefficient. This difference can stem from two factors. First, as the membrane partition coefficient decreases, a denser build-up of the solute particles is formed near the wall, leading to an increase in $C_{p,r=R_f}$ in the denominator of Equation (15), providing more solute to permeate through the remaining pores. In addition, the permeating solute concentration on the inner wall ($C_{p,r=R_f}$) is not uniformly distributed through the z-dimension of the membrane, and, therefore, the permeate concentration at the permeate side does not exactly resemble the membrane partition coefficient behavior.

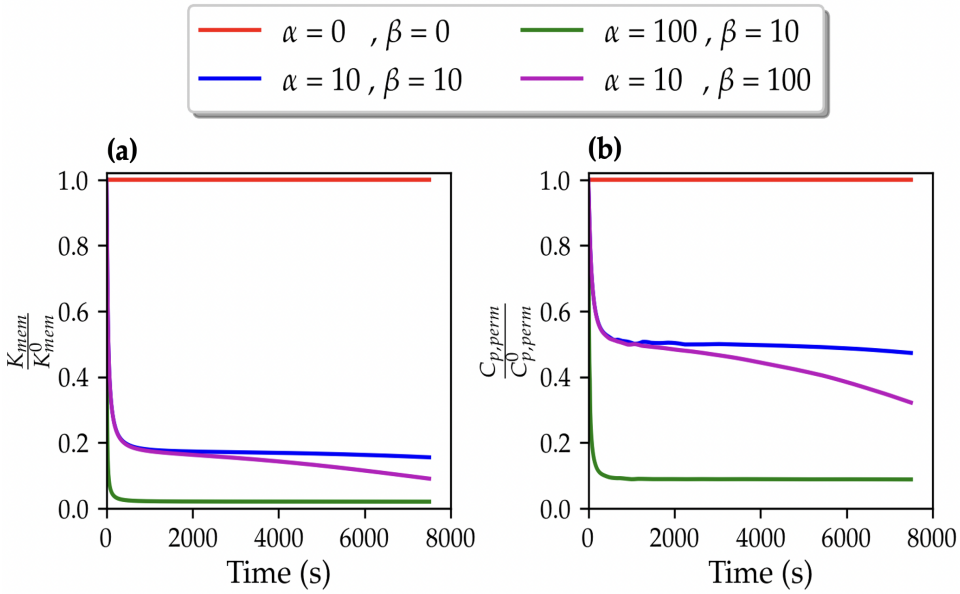

Figure 9. Variation in (**a**) $\frac{K_{perm}}{K^0_{perm}}$ and (**b**) $\frac{C_{p,perm}}{C^0_{p,perm}}$ over time. K^0_{perm} and $C^0_{p,perm}$ are membrane partition coefficient and the permeate concentration obtained at the initial time step, respectively.

Ultimately, to assess the predictive capability of our model for the permeate concentration profile, we conducted the optimization of the α and β parameters to fit the calculated permeate concentration profile to the experimental data obtained for three different inlet concentrations. The experimental data were drawn from Figure S2 of reference [19], where C_{feed} denotes the combined graphene and non-exfoliated graphite content of the feed. In our simulations, we assumed the graphene compounds and non-exfoliated graphites accounted for 25 wt% and 75 wt% of the C_{feed}, respectively. As displayed in Figure 10, the simulation yielded a satisfactory correlation with the simulations with an MAE of 0.0002, 0.0003, and 0.0022 g/L for C_{feed} values of 0.05, 0.1, and 0.3 g/L, respectively. Additionally, we compared the total amount of filtered permeating solute predicted by our model to the experimental data. The comparison revealed strong agreement, with absolute error values of 0.0003, 0.0005, and 0.0003 g/L for C_{feed} values of 0.05, 0.1, and 0.3 g/L, respectively.

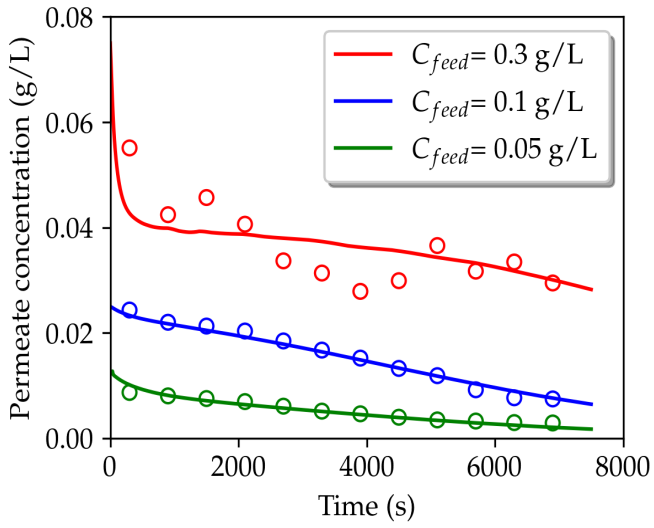

Figure 10. Variation in permeate concentration over time obtained from experiments and simulations using optimized α and β parameters for different inlet concentrations, e.g., 0.3, 0.1, and 0.05 g/L. The circles and lines highlight the experimental and simulation results, respectively.

As elaborated in the Methods section, the α and β parameters represent the relative number of rejected solute particles compared with the rejected solvent molecules. Therefore, these parameters are inherently size- and concentration-dependent. We speculate that both the α and β values ascend with increasing concentrations. However, the optimized parameters for different concentrations failed to exhibit a meaningful correlation (Table 2). This lack of pattern may be attributed to our approach to obtain the α and β parameters. As Equation (15) suggests, the partition coefficient is impacted by the interplay between the resistance parameters and the α and β parameters. For the three different feed concentration systems studied, we adopted similar values for the resistance parameters, such as $R_{pol,ss}$, k_{pol}, R_{ads}, etc., while these fouling-dependent parameters might vary upon changes in the foulant content of the system. Therefore, although our model demonstrated the capability to accurately predict the permeate concentration profile of 2D materials, in order to determine concentration-dependent α and β parameters, it is essential to target multiple experimental TMP and permeate concentration profiles over time. These profiles will serve as the basis for deriving the relationship between solute rejection behavior and varying concentrations. This approach can be explored in future studies to enhance our understanding of the concentration-dependent effects on fouling parameters.

Table 2. Comparison of the total permeate concentration obtained from the simulations and experiments.

C_{feed} (g/L)	α	β	Total Permeate Concentration (g/L)	
			Simulation	**Experiment [19]**
0.05	6	400	0.0050	0.0053
0.1	1	250	0.0151	0.0156
0.3	9	70	0.0363	0.0360

4. Conclusions

In this study, we presented a CFD model for the filtration of 2D materials using hollow fiber membrane filtration. Navier–Stokes and mass conservation equations were integrated into the model to numerically solve the flow and concentration behaviors in the system. The fouling phenomena were coupled to the model through the Darcy relation and use of the resistance-in-series technique. The resistance contributions were assumed to arise from concentration polarization and the combined effects of pore reduction and cake formation on the inner surface of the membrane. Additionally, we proposed that fouling of graphitic layered structures enhances the membrane surface wettability, leading to an increment in solvent permeation through the pores. The wettability effect was incorporated into the model by defining the R'_{wet} term and combined with the other resistance terms used in the Darcy relation. The model yielded an excellent fit with the experimental transmembrane pressure (TMP) data with a Mean Absolute Error of 0.007 psi.

Furthermore, the model was also armed with a fouling-dependent membrane partition coefficient for the permeating solute, which formulated the effects of fouling regimes on the rejection of the solute using the definition of the α and β parameters. Our results revealed that the α parameter determines the level of the rejection during the concentration polarization regime, while the β parameter controls the rejection of the permeating solute during the cake formation stage. The optimized α and β parameters enabled the model to predict the experimental permeate concentration profile with Mean Absolute Errors of 0.0002, 0.0003, and 0.0022 g/L for three different feed concentrations (C_{feed}) of 0.05, 0.1, and 0.3 g/L, respectively. The current model initiates the modeling of isolation of 2D materials using hollow fiber membranes, paving the way for further advancements in the eco-friendly production of 2D materials through filtration techniques.

Author Contributions: Conceptualization, A.E. and S.C.; methodology, A.E.; software, A.E.; validation, A.E.; formal analysis, A.E.; investigation, A.E.; resources, A.E. and S.C.; data curation, A.E.; writing—original draft preparation, A.E.; writing—review and editing, A.E.; visualization, A.E.; supervision, S.C.; project administration, S.C.; funding acquisition, S.C. All authors have read and agreed to the published version of the manuscript.

Funding: This research, including APC, was funded by National Science Foundation (NSF) through the Future Manufacturing MADE-PUBLIC program (grant number 2037026)

Data Availability Statement: The data presented in this study can be found in Section 2.4 and Table 1.

Acknowledgments: We acknowledge with gratitude the expert assistance by Mark Hersam's research team at the Materials Science and Engineering Department of Northwestern University, which was crucial for accurately modeling their experimental filtration setup.

Conflicts of Interest: The authors declare no conflict of interest.

Nomenclature

symbols

C_{feed}	feed concentration of combined fouling and permeating particles (g/L)
D_f	diameter of the fiber (m)
C_f	fouling solute concentration (g/L)
C_p	permeating solute concentration (g/L)
$C_{p,perm}$	permeating solute concentration at the permeate stream (g/L)
$C^0_{p,perm}$	permeating solute concentration at the permeate stream (g/L) at the initial time step
D_f	diffusion coefficient of fouling particle (m^2/s)
D_p	diffusion coefficient of permeating particle (m^2/s)
J_p	mass flux of permeating particles through the membrane (g/(m·s))
k_{pol}	polarization time constant coefficient (s g/L)
k_{wet}	wettability effect time constant coefficient (s g/L)
K_{mem}	membrane partition coefficient
K^0_{mem}	membrane partition coefficient at the initial time step
k^0_{perm}	initial membrane partition coefficient
L_f	length of the fiber (m)
P_{in}	inlet hollow fiber pressure (Pa)
P_{ret}	retentate pressure (Pa)
P_{perm}	permeate pressure (Pa)
N_f	number of fibers
Q_{inlet}	inlet flow rate (m^3/s)
Q_{perm}	experimentally set permeate flow rate (m^3/s)
R_f	radius of the fiber (m)
$R_{cake,ss}$	steady-state cake formation resistance (m^{-1})
R_m	clean membrane resistance (m^{-1})
$R_{pol,ss}$	steady-state polarization resistance (m^{-1})
$R'_{wet,ss}$	steady state wettability effect on reducing the resistance(m^{-1})
Re	Reynolds number (dimensionless)
u_r	fluid velocity in the r-direction of the domain (m/s)
u_z	fluid velocity in the z-direction of the domain (m/s)
U_{perm}	permeate velocity (m/s)
U_{inlet}	inlet mean velocity (m/s)

Greek letters

α	dimensionless parameter in the partition coefficient, Equation (15)
β	dimensionless parameter in the partition coefficient, Equation (15)
μ	dynamic viscosity of the fluid (Pa · s)
ρ	density of the fluid (kg/m^3)
τ_{pol}	polarization time constant (s)
τ_{cake}	cake formation time constant (s)
τ'_{wet}	wettability effect time constant (s)

References

1. Zhao, S.; Zou, L.; Tang, C.Y.; Mulcahy, D. Recent developments in forward osmosis: Opportunities and challenges. *J. Membr. Sci.* **2012**, *396*, 1–21. [CrossRef]
2. Wang, P.; Chung, T.S. Recent advances in membrane distillation processes: Membrane development, configuration design and application exploring. *J. Membr. Sci.* **2015**, *474*, 39–56. [CrossRef]
3. Bera, S.P.; Godhaniya, M.; Kothari, C. Emerging and advanced membrane technology for wastewater treatment: A review. *J. Basic Microbiol.* **2022**, *62*, 245–259. [CrossRef] [PubMed]
4. Lasseuguette, E.; Comesaña-Gándara, B. Polymer Membranes for Gas Separation. *Membranes* **2022**, *12*, 207. [CrossRef]
5. Dai, Y.; Niu, Z.; Luo, W.; Wang, Y.; Mu, P.; Li, J. A review on the recent advances in composite membranes for CO_2 capture processes. *Sep. Purif. Technol.* **2023**, *307*, 122752. [CrossRef]
6. Nazir, A.; Khan, K.; Maan, A.; Zia, R.; Giorno, L.; Schroën, K. Membrane separation technology for the recovery of nutraceuticals from food industrial streams. *Trends Food Sci. Technol.* **2019**, *86*, 426–438. [CrossRef]
7. Conidi, C.; Castro-Muñoz, R.; Cassano, A. Membrane-based operations in the fruit juice processing industry: A review. *Beverages* **2020**, *6*, 18. [CrossRef]
8. Reig, M.; Vecino, X.; Cortina, J.L. Use of membrane technologies in dairy industry: An overview. *Foods* **2021**, *10*, 2768. [CrossRef] [PubMed]
9. Hooshyar, S.; Yoshikawa, H.N.; Mirbod, P. The impact of imposed Couette flow on the stability of pressure-driven flows over porous surfaces. *J. Eng. Math.* **2022**, *132*, 15. [CrossRef]
10. Lin, H.; Gao, W.; Meng, F.; Liao, B.Q.; Leung, K.T.; Zhao, L.; Chen, J.; Hong, H. Membrane bioreactors for industrial wastewater treatment: A critical review. *Crit. Rev. Environ. Sci. Technol.* **2012**, *42*, 677–740. [CrossRef]
11. Vanneste, J.; Ormerod, D.; Theys, G.; Gool, D.V.; Camp, B.V.; Darvishmanesh, S.; der Bruggen, B.V. Towards high resolution membrane-based pharmaceutical separations. *J. Chem. Technol. Biotechnol.* **2013**, *88*, 98–108. [CrossRef]
12. Rana, D.; Matsuura, T. Surface modifications for antifouling membranes. *Chem. Rev.* **2010**, *110*, 2448–2471. [CrossRef]
13. Wang, Y.N.; Tang, C.Y. Nanofiltration membrane fouling by oppositely charged macromolecules: Investigation on flux behavior, foulant mass deposition, and solute rejection. *Environ. Sci. Technol.* **2011**, *45*, 8941–8947. [CrossRef]
14. Nthunya, L.N.; Bopape, M.F.; Mahlangu, O.T.; Mamba, B.B.; der Bruggen, B.V.; Quist-Jensen, C.A.; Richards, H. Fouling, performance and cost analysis of membrane-based water desalination technologies: A critical review. *J. Environ. Manag.* **2022**, *301*, 113922. [CrossRef]
15. Kovacs, D.J.; Li, Z.; Baetz, B.W.; Hong, Y.; Donnaz, S.; Zhao, X.; Zhou, P.; Ding, H.; Dong, Q. Membrane fouling prediction and uncertainty analysis using machine learning: A wastewater treatment plant case study. *J. Membr. Sci.* **2022**, *660*, 120817. [CrossRef]
16. Pervez, M.N.; Mishu, M.R.; Stylios, G.K.; Hasan, S.W.; Zhao, Y.; Cai, Y.; Zarra, T.; Belgiorno, V.; Naddeo, V. Sustainable treatment of food industry wastewater using membrane technology: A short review. *Water* **2021**, *13*, 3450. [CrossRef]
17. Zaman, N.K.; Rohani, R.; Mohammad, A.W.; Isloor, A.M.; Jahim, J.M. Investigation of succinic acid recovery from aqueous solution and fermentation broth using polyimide nanofiltration membrane. *J. Environ. Chem. Eng.* **2020**, *8*, 101895. [CrossRef]
18. He, Y.; Bagley, D.M.; Leung, K.T.; Liss, S.N.; Liao, B.Q. Recent advances in membrane technologies for biorefining and bioenergy production. *Biotechnol. Adv.* **2012**, *30*, 817–858. [CrossRef]
19. Downing, J.R.; Diaz-Arauzo, S.; Chaney, L.E.; Tsai, D.; Hui, J.; Seo, J.W.T.; Cohen, D.R.; Dango, M.; Zhang, J.; Williams, N.X.; et al. Centrifuge-Free Separation of Solution-Exfoliated 2D Nanosheets via Cross-Flow Filtration. *Adv. Mater.* **2023**, *35*, e2212042. [CrossRef]
20. Rajabzadeh, A.R. Membrane Fouling During Hollow Fiber Ultrafiltration of Protein Solutions: Computational Fluid Modeling and Physicochemical Properties. Ph.D. Thesis, University of Waterloo, Waterloo, ON, Canada, 2010.
21. Quezada, C.; Estay, H.; Cassano, A.; Troncoso, E.; Ruby-Figueroa, R. Prediction of permeate flux in ultrafiltration processes: A review of modeling approaches. *Membranes* **2021**, *11*, 368. [CrossRef]
22. Kumar, N.S.K.; Yea, M.K.; Cheryan, M. Ultrafiltration of soy protein concentrate: Performance and modelling of spiral and tubular polymeric modules. *J. Membr. Sci.* **2004**, *244*, 235–242. [CrossRef]
23. Marcos, B.; Moresoli, C.; Skorepova, J.; Vaughan, B. CFD modeling of a transient hollow fiber ultrafiltration system for protein concentration. *J. Membr. Sci.* **2009**, *337*, 136–144. [CrossRef]
24. Das, B.; Bhattacharjee, S.; Bhattacharjee, C. Recovery of Whey Proteins and Enzymatic Hydrolysis of Lactose Derived from Casein Whey Using a Tangential Flow Ultrafiltration Module. *J. Inst. Eng. (India) Ser. E* **2013**, *94*, 79–84. [CrossRef]
25. Mondal, M.; De, S. Purification of Polyphenols from Green Tea Leaves and Performance Prediction Using the Blend Hollow Fiber Ultrafiltration Membrane. *Food Bioprocess Technol.* **2019**, *12*, 933–953. [CrossRef]
26. Hosseini, M.K.; Liu, L.; Hosseini, P.K.; Lee, K.; Miao, J. Performance evaluation of a pilot-scale membrane filtration system for oily wastewater treatment: CFD modeling and scale-up design. *J. Water Process. Eng.* **2023**, *52*, 103570. [CrossRef]
27. Straub, A.P.; Bergsman, D.S.; Getachew, B.A.; Leahy, L.M.; Patil, J.J.; Ferralis, N.; Grossman, J.C. Highly Conductive and Permeable Nanocomposite Ultrafiltration Membranes Using Laser-Reduced Graphene Oxide. *Nano Lett.* **2021**, *21*, 2429–2435. [CrossRef] [PubMed]
28. Ding, A.; Ren, Z.; Zhang, Y.; Ma, J.; Bai, L.; Wang, B.; Cheng, X. Evaluations of holey graphene oxide modified ultrafiltration membrane and the performance for water purification. *Chemosphere* **2021**, *285*, 131459. [CrossRef]

29. Kumar, M.; Sreedhar, N.; Thomas, N.; Mavukkandy, M.; Ismail, R.A.; Aminabhavi, T.M.; Arafat, H.A. Polydopamine-coated graphene oxide nanosheets embedded in sulfonated poly(ether sulfone) hybrid UF membranes with superior antifouling properties for water treatment. *Chem. Eng. J.* **2022**, *433*, 133526. [CrossRef]
30. Likhi, F.H.; Singh, M.; Chavan, S.V.; Cao, T.; Shanbedi, M.; Karim, A. Effects of Film Confinement on Dielectric and Electrical Properties of Graphene Oxide and Reduced Graphene Oxide-Based Polymer Nanocomposites: Implications for Energy Storage. *ACS Appl. Nano Mater.* **2023**, *6*, 11699–11714. [CrossRef]
31. Choi, W.; Choi, J.; Bang, J.; Lee, J.H. Layer-by-layer assembly of graphene oxide nanosheets on polyamide membranes for durable reverse-osmosis applications. *ACS Appl. Mater. Interfaces* **2013**, *5*, 12510–12519. [CrossRef]
32. Lee, J.; Chae, H.R.; Won, Y.J.; Lee, K.; Lee, C.H.; Lee, H.H.; Kim, I.C.; Lee, J.-M. Graphene oxide nanoplatelets composite membrane with hydrophilic and antifouling properties for wastewater treatment. *J. Membr. Sci.* **2013**, *448*, 223–230. [CrossRef]
33. Miao, W.; Li, Z.K.; Yan, X.; Guo, Y.J.; Lang, W.Z. Improved ultrafiltration performance and chlorine resistance of PVDF hollow fiber membranes via doping with sulfonated graphene oxide. *Chem. Eng. J.* **2017**, *317*, 901–912. [CrossRef]
34. Yu, C.; Song, Y.S. Enhancing energy harvesting efficiency of form stable phase change materials by decreasing surface roughness. *J. Energy Storage* **2023**, *58*, 106360. [CrossRef]
35. Lundgren, M.; Allan, N.L.; Cosgrove, T.; George, N. Wetting of water and water/ethanol droplets on a non-polar surface: A molecular dynamics study. *Langmuir* **2002**, *18*, 10462–10466. [CrossRef]
36. Metya, A.K.; Khan, S.; Singh, J.K. Wetting transition of the ethanol-water droplet on smooth and textured surfaces. *J. Phys. Chem. C* **2014**, *118*, 4113–4121. [CrossRef]
37. Fang, H.H.; Shi, X. Pore fouling of microfiltration membranes by activated sludge. *J. Membr. Sci.* **2005**, *264*, 161–166. [CrossRef]
38. Yi, Z.; Zhu, L.P.; Xu, Y.Y.; Zhao, Y.F.; Ma, X.T.; Zhu, B.K. Polysulfone-based amphiphilic polymer for hydrophilicity and fouling-resistant modification of polyethersulfone membranes. *J. Membr. Sci.* **2010**, *365*, 25–33. [CrossRef]
39. Li, X.; Li, J.; Wang, J.; Wang, H.; He, B.; Zhang, H.; Guo, W.; Ngo, H.H. Experimental investigation of local flux distribution and fouling behavior in double-end and dead-end submerged hollow fiber membrane modules. *J. Membr. Sci.* **2014**, *453*, 18–26. [CrossRef]
40. Gonalves, F.A.; Trindade, A.R.; Costa, C.S.; Bernardo, J.C.; Johnson, I.; Fonseca, I.M.; Ferreira, A.G. PVT, viscosity, and surface tension of ethanol: New measurements and literature data evaluation. *J. Chem. Thermodyn.* **2010**, *42*, 1039–1049. [CrossRef]